

Soft Matter

Accepted Manuscript



This is an *Accepted Manuscript*, which has been through the Royal Society of Chemistry peer review process and has been accepted for publication.

Accepted Manuscripts are published online shortly after acceptance, before technical editing, formatting and proof reading. Using this free service, authors can make their results available to the community, in citable form, before we publish the edited article. We will replace this *Accepted Manuscript* with the edited and formatted *Advance Article* as soon as it is available.

You can find more information about *Accepted Manuscripts* in the [Information for Authors](#).

Please note that technical editing may introduce minor changes to the text and/or graphics, which may alter content. The journal's standard [Terms & Conditions](#) and the [Ethical guidelines](#) still apply. In no event shall the Royal Society of Chemistry be held responsible for any errors or omissions in this *Accepted Manuscript* or any consequences arising from the use of any information it contains.



Soft Matter

ARTICLE

Influence of fluid flow on stability and wetting transition of submerged superhydrophobic surfaces

Received 00th January 20xx,
Accepted 00th January 20xx

DOI: 10.1039/x0xx00000x

www.rsc.org/

Yaolei Xiang,^a Yahui Xue,^a Pengyu Lv,^a Dandan Li^a and Hailing Duan^{*,a,b}

Superhydrophobic surfaces have attracted great attention for drag reduction application. However, these surfaces are subject to instabilities, especially under fluid flow. In this work, we in situ examine the stability and wetting transition of underwater superhydrophobicity in laminar flow conditions by confocal microscopy. The absolute liquid pressure in the flow channel is regulated to acquire the pinned Cassie-Baxter and depinned metastable states. The subsequent dynamic evolution of the meniscus morphology in the two states under shear flow is monitored. It is revealed that fluid flow does not affect the pressure-mediated equilibrium states but accelerates the air exchange between entrapped air cavities and bulk water. A diffusion-based model with varied effective diffusion length is used to interpret the experimental data, which show a good agreement. The Sherwood number representing the convection-enhanced mass transfer coefficient is extracted from the data, and is found to follow a classic 1/3-power-law relation with the Reynolds number as has been discovered in channel flows with diffusive boundary conditions. The current work paves the way for designing durable superhydrophobic surfaces under flow conditions.

Introduction

Bioinspired superhydrophobic surfaces find extensive applications in many fields such as self-cleaning, drag reduction and heat transfer.¹⁻⁶ The functionality of these surfaces relies on maintaining a large area fraction of liquid-air interfaces on hydrophobic textures, i.e., the nonwetted Cassie-Baxter (CB) state. However, the failure of superhydrophobicity may be induced by physical mechanisms such as pressurization, impact, and evaporation, leading to the fully wetted Wenzel state.⁷⁻⁹ In particular for the application of underwater superhydrophobicity in fluidic devices or marine vessels for drag reduction purpose, it requires a better understanding of the wetting behavior.

When superhydrophobic surfaces are submerged underwater, the liquid-air interfaces may retain a depinned metastable state as a result of the resistance produced by air compressibility in the entrapped cavities, which enhances the critical wetting transition pressure.^{10,11} On the other hand, the air exchange between the entrapped air cavities and the surrounding bulk water could gradually cause the wetting transition of underwater superhydrophobicity, harming its durable functioning.¹²⁻¹⁴

This situation is deteriorated when these surfaces are subject to fluid flow. A convection-diffusion regime greatly

accelerates the air exchange rate and reduces the longevity of superhydrophobic surfaces.^{16,17} Optical techniques such as light reflection have been employed to directly observe the dynamic CB-to-Wenzel transition process in flow conditions.^{18, 19} However, there still lack highly resolved measurements to reach a quantitative understanding of the longevity-dependence on the flow rate, which benefits the design of durable superhydrophobic surfaces for drag reduction applications.

In this article, we aim to clarify the underlying mechanisms of the stability and wetting transition on submerged superhydrophobic surfaces subject to low-Reynolds-number fluid flows. Note that the entrapped air bubbles on microstructured surfaces are deformable under relatively high-shear flow, which also affects the mass transport and thus the wetting states.¹⁵ Here, we focus on low-shear flows when the bubbles stay spherical, which rules out the effect of bubble deformation. Following our previous work,^{14, 20} we take advantage of laser scanning confocal microscopy to *in situ* monitor and quantify the morphology evolution of entrapped air cavities on structured hydrophobic surfaces in a flow field with different liquid pressures. The absolute liquid pressure in the flow channel is regulated to obtain different initial wetting states, and subsequently, the dynamic evolution of these states under shear flow is investigated. A diffusion-based model developed in Ref. [14] is adapted to interpret the experimental results. The Reynolds number-dependence of the convection-enhanced mass transfer coefficient, as represented by the Sherwood number, is analyzed and compared with classic results for internal channel flows with diffusive boundary conditions.

^a State Key Laboratory for Turbulence and Complex Systems, Department of Mechanics and Engineering Science, College of Engineering, Peking University, Beijing 100871, People's Republic of China. E-mail: hlduan@pku.edu.cn

^b HEDPS, Center for Applied Physics and Technology, BIC-ESAT, Peking University, Beijing 100871, People's Republic of China

Experiment

The experiment setup for direct observation of the dynamic progress of liquid-air interfaces on structured hydrophobic surfaces under fluid flow is shown in Fig. 1a. Samples patterned with cylindrical micropores were fabricated on silicon substrates after further hydrophobization by chemical vapor deposition of self-assembled monolayers of fluorosilane. The pore radius (r) and height (H) are 25 and 40 μm , respectively. The sample was fixed at the bottom of a flow cell (i.e., a box made from plexiglass) with a rectangularly-shaped cross-section (1.5 mm \times 15 mm in depth and width) and length of 85 mm. Two thin and long tubes (5 mm \times 1.5 m in radius and length) were used to connect the flow cell with a sealed water tank for water circulation. The water tank is a sealed plexiglass box with the size of 10 cm \times 10 cm in cross-section and 55 cm in height and there are 2 holes on the roof of the tank which are used to change and monitor the air pressure above water in the tank. The flow cell was gradually filled with water by controlling a switch. Prior to each experiment, the water in the tank had been equilibrated in a clean ambient environment over days. The absolute liquid pressure (p_L) in the flow cell is tunable through the inlet air pressure and the water level (H_w) in the tank above the sample surface. The overpressure relative to the atmospheric pressure (p_0) is denoted by $\Delta p = p_L - p_0$. In all the experiments below, H_w was kept at 70 mm, and Δp was solely regulated through the inlet air pressure, which was monitored by a pressure transmitter. The pressure drop across the flow channel depends on the magnitude of the flow rate, and is relatively small for low-Reynolds-number flows. The control of the flow rate (f) up to 20 ml/min in the flow system was realized by a precise peristaltic pump with the uncertainty kept within 1%. The highest flow rate ($f = 20$ mL/min) corresponds to an maximum average flow velocity (U) of 14.8 mm/s in the flow channel, and a Reynolds number (Re) of 22, according to the definition, $Re = \rho U d / \mu$, where ρ and μ are the liquid density and viscosity, respectively, and d is the depth of the flow channel, equal to 1.5 mm.

The observation of the meniscus morphology on the sample surface in fluid flow was achieved through a window fabricated at the roof of the flow cell right above the center of sample (see Fig. 1b), which was tightly sealed by a piece of thin coverglass with high transparency. An upright laser scanning confocal microscope (LSCM 710, Carl Zeiss, Germany) using a 20 \times water-immersion objective (NA=1.0) with a 1.8 mm working distance was employed to probe the morphology of the liquid-air interfaces through the observation window. The objective was immersed in a large droplet sitting on top of the coverglass so as to avoid light refraction although the recorded laser intensity was weakened slightly. A quick line-scanning mode across the pore diameter was used to capture the transient morphology of the moving meniscus. A low concentration (~ 1 $\mu\text{g/mL}$) of Rhodamine B (95%, J&K Scientific, China) was used to label the deionized water so as to obtain better image contrast for the liquid-air interfaces, where those fluorescent molecules are

preferentially adsorbed but without significantly changing the liquid properties (e.g., surface tension and viscosity).

Results

Depending on the liquid pressure, the entrapped meniscus on structured hydrophobic surfaces may retain a pinned CB state or depinned metastable state,^{10, 14} as schematically shown in Figs. 2a and 2e, respectively. The feasibility of the above experiment system as illustrated in Fig. 1a was first demonstrated by directly observing the two different wetting states under hydrostatic pressures in still water. Typical LSCM images are shown in Figs. 2b and 2f. At a vanishing overpressure (e.g., $\Delta p = 0.7$ kPa, i.e., only the liquid pressure in the tank), the liquid-air interface was almost planar and capable of persisting in the pinned CB state for hours, consistent with the experimental observation in Ref. [21]. The liquid-air interface became concave when Δp was elevated to 11.7 kPa. After storage at this pressure for 10 min, the meniscus started to depin from the pore corners (Fig. 2f). This process was mediated by the air diffusion from the entrapped air cavities into the bulk water, which has been systematically investigated in Ref. [14].

The dynamic progression of the meniscus subject to different fluid flow rates is the main focus of the present work. The absolute liquid pressure in the flow channel was shown to affect the bubble morphology evolution.²² We chose the pinned CB state (i.e., Fig. 2b) and the depinned metastable state (i.e., Fig. 2f) as the initial ones, and subsequently applied different flow rates to investigate the evolution of the two different states under corresponding pressure conditions. Representative sequences of the images of the evolving menisci at a constant flow rate of $f = 15$ mL/min are shown in Figs. 2b-d and Figs. 2f-h. It is seen that the menisci indeed stay in a spherical shape in the present shear flow condition. Moreover, it is found that the meniscus curvature at $\Delta p = 0.7$ kPa remained unchanged even under a shear flow (Fig. 2b). When the overpressure was elevated to 2.7 kPa ten min later while maintaining the shear flow, the meniscus immediately became slightly concave (Fig. 2c), and then gradually sagged into the pore with increasing curvature but remained pinned at pore corners (Fig. 2d). Negligible change was observed approximately 20 min after the pressure elevation, indicating a new equilibrium state was being established. In contrast, at $\Delta p = 11.7$ kPa, the depinned meniscus was driven to slid faster on the sidewalls by the fluid flow (Figs. 2f-h) until the pore bottom was touched, which triggered the wetting transition to a fully wetted Wenzel state.

The contact angle (θ) and sagging depth (h) of the meniscus (see Figs. 2a and 2e) were directly measured from the image sequences showing the evolution of the meniscus profile at different flow rates or Reynolds numbers (Re), in order to quantitatively examine the dynamic wetting transition process. The resulting values as a function of time (t) are plotted in Figs. 3a and 3b, respectively, which exhibit distinctly different characters. At relatively lower pressure,

the meniscus is sustained in a pinned CB state irrespective with the Reynolds number, which just affects the transition speed between the two equilibrium states as indicated by the constant or slightly changed θ . However, for relatively larger liquid pressure, the sagging depth (h), normalized by H , increases linearly with time until the collapse of the meniscus, and the slope increases with the Reynolds number, implying the shear flow accelerates the wetting transition from a CB to Wenzel state on structured hydrophobic surfaces. Only those data for the values of h/H lower than 0.8 are shown in Fig. 3b, as beyond the critical value the meniscus profile could be hardly distinguished from the reflection signal by the pore bottom.²³

Discussion

The above experiment observations shed light on the dependence of CB-to-Wenzel wetting transition on fluid flow. In what follows, we demonstrate the transition process is dominated by a convection-diffusion mechanism and mediated by the liquid pressure. Consider a flow channel with only the bottom patterned with hydrophobic micropores, as schematically shown in Fig. 1b. The air diffusion from entrapped cavities into bulk water is controlled by a density gradient across a poorly-mixed region near the sample surface.²⁴⁻²⁶ The governing equation for the molecular flux reads,¹⁴

$$\frac{dN(t)}{dt} = -\frac{A(t)D_G}{lK_G}[p_G(t) - sp_{G0}], \quad (1)$$

where N and p_G are molecular number and gas partial pressure in the cavity, respectively, A is liquid-air interfacial area and equals $2\pi r^2(1 - \sin\theta)/\cos^2\theta$, p_{G0} is gas partial pressure in the atmosphere, and D_G and K_G are diffusion coefficient and Henry's constant, respectively. The assumption of a quasi-mechanical equilibrium of the meniscus yields $p_G = p_L - p_V + 2\gamma\cos\theta/r$, following the Laplace equation, where γ is surface tension, and p_V is vapor pressure.¹⁰ The cavity volume is denoted by V , equal to $\pi r^2(H - h) + \pi r^3(2 - 3\sin\theta + \sin^3\theta)/(3\cos^3\theta)$. Then, N is related to p_G by the ideal gas law, $N = p_G V/(RT)$, where R and T are universal gas constant and room temperature (23°C), respectively. For freshly immersed samples, the initial molar number is taken as $N(0) = p_{G0}V_H/(RT)$, where V_H is the net cavity volume and equals $\pi r^2 H$.

In Eq. 1, s represents the gas saturation degree in the bulk water, approximately equal to 1.0 since the bulk water is equilibrated in the atmosphere, and l is the effective diffusion length, which can be extracted from experimental data. Under a hydrostatic circumstance, l is uniform across the sample surface. On the other hand, l is distributed in the internal flow field along the position (x) from the leading edge of the sample, and varies with the fluid flow rate. Here, we focus on the variation of l with the flow rate (or Reynolds number) at a fixed position, e.g., the middle of the sample surface (see Fig. 1b).

Note that in the pinned CB state (Fig. 2a), θ varies but the meniscus keeps pinned at the sharp pore edge while in the depinned metastable state (Fig. 2e), θ keeps constant and equals the advancing contact angle (θ_a , approximately 120°), but h varies. In particular for the depinned metastable state, a similarity law has been discovered, which shows the linear variation of h with time (t) under different hydrostatic pressures.¹⁴ Theoretical predictions by Eq. 1 for the CB and depinned metastable states are included as lines in Figs. 3a and 3b, respectively. For both states, a good agreement between the data and the prediction is found for various Reynolds numbers. The only unknown parameter involved in the calculation is l , which was obtained by fitting the experiment data. For example, l is obtained as $60 \pm 5 \mu\text{m}$, $78 \pm 3 \mu\text{m}$, and $120 \pm 12 \mu\text{m}$ for $Re = 16.68$, 8.34, and 2.08 in the pinned state respectively, indicating the effective diffusion length decreases with the Reynolds number. The variation of the resultant l with Re is analyzed in detail below.

We remark that the internal flow in the extended channel can be considered to be two dimensional (2D) due to the high aspect ratio of the channel cross-section (10:1). As shown in Fig. 1b, for well-developed 2D channel flows with symmetric no-slip boundary conditions, the velocity profile (u) across the cross-sectional direction (y) shows a parabolic distribution. On the other hand, bubble mattresses on the structured sample surface at the bottom may induce liquid slippage, which disturbs the parabolic flow. In order to evaluate the slip effect on the sample surface, we recall the scaling argument of liquid slip on a surface distributed with 2D free-slip disks, which shows that the effective slip length (b) is proportional to $8r\beta/9\pi(1-\beta)$, where β is the area fraction of the disks.²⁷ Given $r = 25 \mu\text{m}$ and $\beta = 0.35$ in the present experiment condition, although the bubble morphology (or curvature) could slightly affect the liquid slippage,^{28, 29} the calculated b on the sample surface is approximately in the scale of $3.8 \mu\text{m}$, which is much smaller than the channel depth ($d = 1.5 \text{ mm}$). Thus, the liquid slip on the sample surface has negligible effect on the overall fluid transport, and for the sake of simplicity, a no-slip boundary condition is still assumed on the bottom surface.

From the above experiment results, it is also seen that the thickness of the diffusion boundary layer adjacent to the sample surface is much smaller than the channel size. Consider the velocity distribution within the thin diffusion boundary layer. It is a good approximation to assume a linear velocity distribution near the wall, that is, $u(y) = 8yU/(3d)$, where U is average velocity in the channel. Then, the simplified governing equation for the convective diffusion is expressed as,³⁰

$$\frac{8U}{3d}y\frac{\partial c}{\partial x} = D_G\frac{\partial^2 c}{\partial y^2}, \quad (2)$$

where c is the gas concentration difference in the flow channel with respect to that in the inflow water. With considering an unlimited diffusion condition, that is, $c_{y \rightarrow \infty} =$

c_0 , and $c_{y=0} = 0$, Eq. (2) can be semi-analytically solved. According to the definition of diffusion rate (j_d),

$$j_d = D_G \left(\frac{\partial c}{\partial y} \right)_{y=0} = D_G \frac{c_0}{l}, \quad (3)$$

the expression for the diffusion length on the slip surface (l) is obtained as³⁰

$$l = 1.03(Sc)^{-1/3}(Re)^{-1/3}(d^2x)^{1/3}, \quad (4)$$

where $Sc = \mu/\rho D_G$ is the Schmidt number.

In order to obtain a more general analysis of the boundary diffusion problem, we recall a dimensionless number used to describe the convection-enhanced diffusive mass transfer, that is, the Sherwood number (or the mass transfer Nusselt number),^{30,31}

$$Sh = \frac{d}{l}, \quad (5)$$

where d is characteristic length scale of the flow field and chosen as the depth of the channel. Then, for a given downstream position (x), combining Eqs. (4) and (5) yields the power-law relation between Sh and Re ,

$$Sh \propto Re^{1/3}. \quad (6)$$

The experimentally measured Sherwood number was calculated with the extracted diffusion length. A logarithmic plot of Sh as a function of Re is shown in Fig. 4. The relation between Sh and Re indeed follows the power-law relation as predicted by Eq. (6). Thus, we experimentally demonstrate that the air diffusion from entrapped air cavities on submerged superhydrophobic surfaces under flow conditions follows a similar principle that has been discovered for classic boundary diffusion problems. The fluid flow decreases the thickness of the diffusion boundary layer, enhances the air partial pressure gradient and thus the mass flow rate.

Conclusions

In this work, we have investigated the stability and wetting transition of structured hydrophobic surfaces under low-Reynolds-number flow conditions. The dynamic evolution of the meniscus morphology in both CB and depinned metastable states was *in situ* monitored by confocal microscopy. It is found that fluid flow does not affect the final equilibrium states of the meniscus, which instead accelerates the air exchange between entrapped air cavities and bulk water by decreasing the effective diffusion length, which enhances the gas-partial-pressure gradient near the sample surface. The equilibrium states are determined by the liquid pressure and the gas saturation degree in the water. This means a durable CB state is sustainable even under flow conditions if a chemical equilibrium though the liquid-air interfaces can be reached. On the other hand, a chemically un-equilibrated, depinned metastable state would exhibit reduced life time. By using the Sherwood number to represent the convective mass transfer coefficient, we discovered a 1/3-power-law relation between Sh and Re , which consists with a classic scaling relation derived for diffusive boundary

problems in flow channels. As has been pointed out by Ref. [21], environmental fluctuation shows strong effects in the equilibrium of the wetting system. Long-time durable superhydrophobic states under high liquid pressure and flow rates will be perused. On the other hand, an optimized design of the topological surface structures also contributes to promoting the longevity of the underwater superhydrophobic state.³² The present work provides a fundamental understanding of the wetting transition mechanism under fluid flow conditions and useful guide for designing superhydrophobicity-based fluidic devices with improved longevity.

Acknowledgements

This work was supported by National Natural Science foundation of China (NSFC) under Grants 11225208 and 11521202.

References

1. K. Liu and L. Jiang, *Annual Review of Materials Research*, 2012, **42**, 231-263.
2. B. Bhushan and Y. C. Jung, *Progress in Materials Science*, 2011, **56**, 1-108.
3. J. P. Rothstein, *Annual Review of Fluid Mechanics*, 2010, **42**, 89-109.
4. P. Zhang and F. Lv, *Energy*, 2015, **82**, 1068-1087.
5. N. Miljkovic and E. N. Wang, *MRS bulletin*, 2013, **38**, 397-406.
6. E. Lauga and H. A. Stone, *Journal of Fluid Mechanics*, 2003, **489**, 55-77.
7. A. Lafuma and D. Quéré, *Nature materials*, 2003, **2**, 457-460.
8. D. Bartolo, F. Bouamrène, É. Verneuil, A. Buguin, P. Silberzan and S. Moulinet, *EPL (Europhysics Letters)*, 2006, **74**, 299.
9. P. Tsai, R. G. Lammertink, M. Wessling and D. Lohse, *Physical review letters*, 2010, **104**, 116102.
10. Y. Xue, S. Chu, P. Lv and H. Duan, *Langmuir*, 2012, **28**, 9440-9450.
11. P. Forsberg, F. Nikolajeff and M. Karlsson, *Soft Matter*, 2011, **7**, 104-109.
12. M. S. Bobji, S. V. Kumar, A. Asthana and R. N. Govardhan, *Langmuir*, 2009, **25**, 12120-12126.
13. R. Poetes, K. Holtzmann, K. Franze and U. Steiner, *Physical review letters*, 2010, **105**, 166104.
14. P. Lv, Y. Xue, Y. Shi, H. Lin and H. Duan, *Physical review letters*, 2014, **112**, 196101.
15. P. Gao and J. J. Feng, *Physics of Fluids*, 2009, **21**(10), 102102.
16. C. Barth, M. Samaha, H. Tafreshi and M. Gad-el-Hak, *International Journal of Flow Control*, 2013, **5**, 79-88.
17. A. S. Haase, E. Karatay, P. A. Tsai and R. G. Lammertink, *Soft matter*, 2013, **9**, 8949-8957.
18. M. A. Samaha, H. V. Tafreshi and M. Gad-el-Hak, *Langmuir*, 2012, **28**, 9759-9766.

Journal Name ARTICLE

19. R. Govardhan, G. Srinivas, A. Asthana and M. Bobji, *Physics of Fluids (1994-present)*, 2009, **21**, 052001.
20. Y. Xue, P. Lv, Y. Liu, Y. Shi, H. Lin and H. Duan, *Physics of Fluids (1994-present)*, 2015, **27**, 092003.
21. M. Xu, G. Sun and C.-J. Kim, *Physical review letters*, 2014, **113**, 136103.
22. D. Dilip, N. K. Jha, R. N. Govardhan and M. Bobji, *Colloids and Surfaces A: Physicochemical and Engineering Aspects*, 2014, **459**, 217-224.
23. P. Lv, Y. Xue, H. Liu, Y. Shi, P. Xi, H. Lin and H. Duan, *Langmuir*, 2015, **31**, 1248-1254.
24. H. Rahn and C. V. Paganelli, *Respiration physiology*, 1968, **5**, 145-164.
25. M. R. Flynn and J. W. Bush, *Journal of Fluid Mechanics*, 2008, **608**, 275-296.
26. B. Emami, A. Hemeda, M. Amrei, A. Luzar, M. Gadel-Hak and H. V. Tafreshi, *Physics of Fluids (1994-present)*, 2013, **25**, 062108.
27. M. Sbragaglia, A. Prosperetti, *Journal of Fluid Mechanics*, 2007, **578**, 435-451.
28. A. Steinberger, C. Cottin-Bizonne, P. Kleimann and E. Charlaix, *Nature Materials*, 2007, **6**(9), 665-668.
29. E. Karatay, A. S. Haase, C. W. Visser, C. Sun, D. Lohse, P. A. Tsai, *Proceedings of the National Academy of Sciences*, 2013, **110**(21): 8422-8426.
30. V. G. Levich and S. Technica, *Physicochemical hydrodynamics*, Prentice-hall Englewood Cliffs, NJ, 1962.
31. S. Pawlowski, P. Sifat, J. G. Crespo and S. Velizarov, *Journal of Membrane Science*, 2014, **471**, 72-83.
32. Y. Liu, L. Moevius, X. Xu, T. Qian, J. M. Yeomans, Z. Wang, *Nature Physics*, 2014, **10**(7), 515-519.

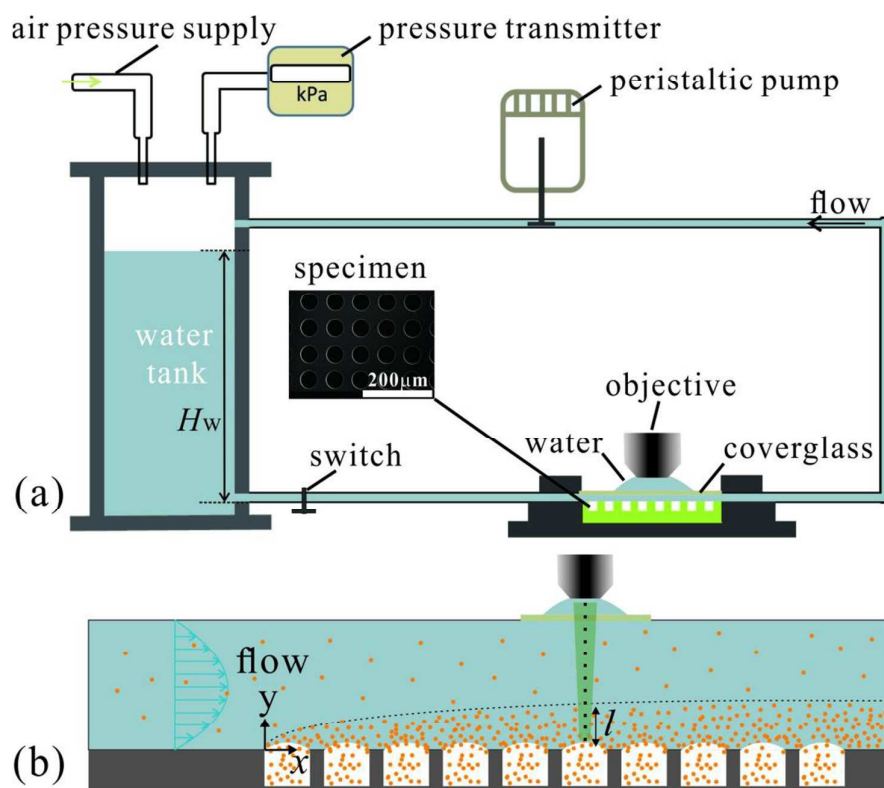


FIG. 1 a) Schematics of the experiment setup. The liquid pressure in the tank is regulated by the inlet air pressure monitored by a pressure transmitter. Confocal microscopy is used to observe the meniscus profile. The flow rate in the channel is controlled by a peristaltic pump. Inset shows the scanning electron microscopic image of the sample sealed at the bottom of the flow channel. (b) Schematics of the diffusion-based model in an internal-flow channel with a superhydrophobic bottom.

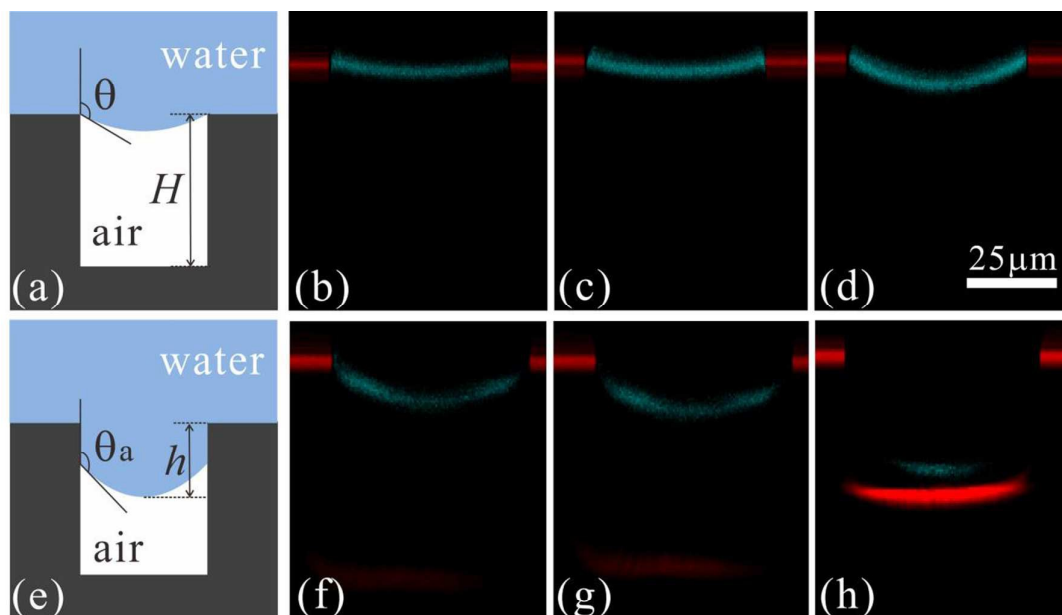


FIG. 2. Schematics and confocal microscopic images of the pinned CB (a, b-d) and depinned metastable (e, f-h) states. The line-scanning images show states at $\Delta p = 0.7$ kPa (b), initially (c) and 20 min later (d) under shear flow at $\Delta p = 2.7$ kPa (top panel); 10 min after fresh immersion in still water (f), 2 min (g) and 10 min (h) later under shear flow at $\Delta p = 11.7$ kPa (bottom panel).

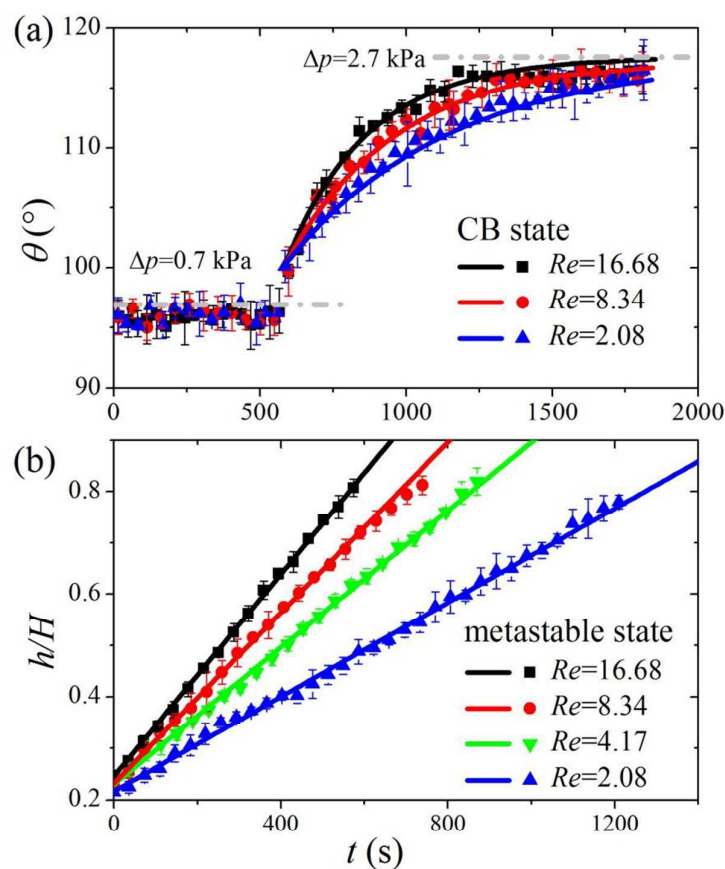


FIG. 3. Experiment results and theoretical predictions of the evolution of the contact angle (θ) at the pinned CB state and the normalized sagging depth (h/H) at the depinned metastable state under different Reynolds numbers. Dots: experiments; Lines: theoretical predictions. In (a), the pressure jumps from $\Delta p = 0.7$ kPa to 2.7 kPa at $t = 600$ s, and dash-dotted lines in (a) show the predicted equilibrium state (i.e., $dN/dt = 0$) at corresponding liquid pressures. In (b), the pressure is held at $\Delta p = 11.7$ kPa.

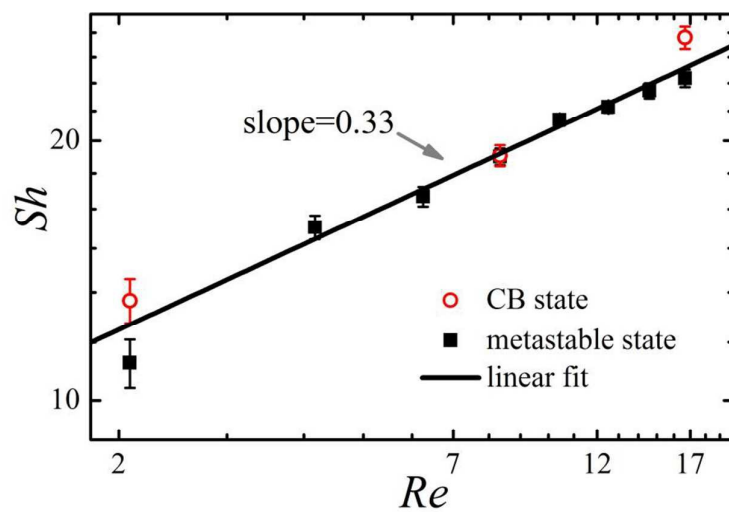


FIG. 4. Variation of the Sherwood number versus the Reynolds number for both CB and metastable states. Dots: experiments; Line: linear fit with a slope of 0.33.